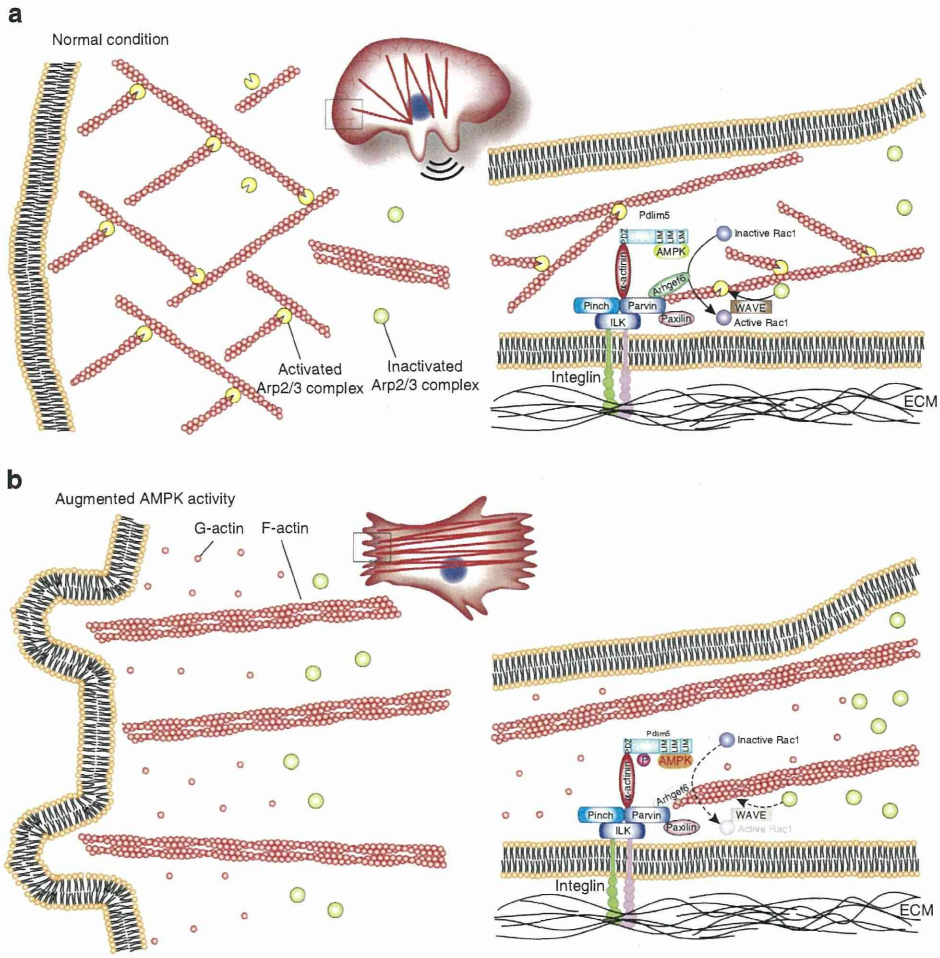

Figure 10 | Model depicting how the Ser177 phosphorylation of Pdlim5 attenuates lamellipodia formation. (**a**) Under normal conditions, Arhgef6 recruited to the IPP complex at the cell periphery activates Rac1, contributing to efficient lamellipodia formation. (**b**) Once AMPK activity is augmented, Ser177 of Pdlim5 is phosphorylated, displacing Arhgef6 from the IPP complex and causing attenuation of lamellipodia. Boxed areas at the cell periphery are expanded, representing views from the top (left) and from the side (right); see text for explanation. ILK, integrin-linked kinase; PINCH, particularly interesting new cysteine-histidine-rich protein; Pdlim5, PDZ and LIM domain 5; WAVE, Wiskott–Aldrich Syndrome protein family verprolin homologous.

expressing Ser177-phosphorylated Pdlim5 might be caused not only by the Arhgef6–Rac1–Arp2/3 complex pathway, but also by other additional mechanisms/pathways including other GEFs/GTPase-activating proteins, other Rho-GTPases (RhoA and Cdc42) and mDia. In addition, the data in Supplementary Fig. 6 demonstrate that KDR/S177A-Pdlim5 cells moved more slowly when treated with AMPK activator, indicating that Pdlim5 is the primary regulator of migration downstream of AMPK, although other pathways are also involved.

We observed a physical and functional association between AMPK, Pdlim5 and F-actin. Pdlim5 binds to AMPK directly through its LIM domain and to F-actin through its PDZ domain, which places AMPK close to F-actin. This interaction seems to rapidly and efficiently transmit AMPK signalling to the actin filament architecture. Thus, we propose that once energy depletion occurs and AMPK is activated, the signal might be transmitted to peripheral actin filaments through this complex, leading to the remodelling of actin-filament architecture and inhibition of cell migration.

A striking feature of the regulation of cell migration by AMPK activity level is that both suppression and augmentation of AMPK inhibit cell migration. Cell migration is a highly complex behaviour that is accomplished by tightly orchestrated dynamic remodelling of the actin cytoskeleton and microtubule network[16]. We previously reported that suppression of AMPK activity inhibits cell migration by hyperstabilizing the microtubule cytoskeleton via dephosphorylation of the microtubule plus-end protein CLIP-170 (ref. 4). In this study, we demonstrated that augmentation of AMPK activity inhibits cell migration by reorganizing actin filaments through phosphorylation of Pdlim5. Thus, the effects of high or low AMPK activity on cell migration may be mediated by completely different mechanisms acting on different substrates, and the two types of substrates may regulate cell migration separately by sensing the level of AMPK activity between two extremes.

Methods

Reagents and antibodies. The following reagents were purchased from the indicated suppliers: AICAR (Sigma-Aldrich), 2-DG (Sigma-Aldrich), A769662 (Santa Cruz Biotechnology) and GST-AMPKα1/β1/γ1 (Carna Biosciences). The following antibodies were purchased from the indicated suppliers: anti-AMPKα (1:2,000; Cell Signaling, 2603), phospho-Thr172 AMPKα (1:2,000; Cell Signaling, 2535), ACC (1:2,000; Cell Signaling, 3676), phospho-Ser79 ACC (1:2,000; Cell Signaling, 3661), anti-paxillin (1:1,000, Zymed Laboratories), anti-α-actinin (D6F6) (1:1,000 for immunoblot; Cell Signaling, 6487), monoclonal anti-α-actinin (1:1,000 for immunostain; Sigma-Aldrich, A5044), anti-Arp2 antibody (1:1,000; Cell Signaling, 3128), anti-Arp3 (FMS338) (1:500 for immunostaining; Abcam, ab49671),

anti-Arpc2 (EPR8533) (1:2,000; Abcam, ab133315), anti-Arhgef6/Cool2/αPIX (C23D2) (1:1,000 for immunoblot; 1:400 for immunostain; Cell Signaling, 4573), anti-Gapdh antibody (1:5,000; Millipore, MAB374), anti-GFP-horseradish peroxidase (HRP) (1:3,000; MBL, 598-7), anti-RFP-HRP (1:3,000; MBL, PM005-7), anti-FLAG M2-HRP (1:5,000; Sigma-Aldrich, A8592), anti-V5-HRP antibody (1:5,000; Life Technologies, R961-25), HRP-coupled goat anti-rabbit (1:8,000; Cappel, 55696), anti-mouse IgG (1:8,000; Cappel, 55550), Alexa Fluor 488- (1:1,000 for staining; Life Technologies, A11029), Alexa Fluor 546- (1:1,000 for staining; Life Technologies, A11003) and Alexa Fluor 568-labelled secondary antibodies (1:1,000 for staining; Life Technologies, A11011), and Alexa Fluor 647 phalloidin (1:100 for staining; Cell Signaling, 8940). Anti-FLAG M2 affinity gel (A2220) and anti-V5 agarose affinity gel (A7345) were from Sigma-Aldrich. We used three different AMPK activators: AICAR is metabolized intracellularly to ZMP (5-aminoimidazole-4-carboxamide-1-β-D-ribofuranotide), an AMP analogue. A769662 is a thienopyridone derivative that acts as an allosteric activator of the AMPK by binding to an alternative site that does not overlap with the AMP-binding site. 2-DG is a non-metabolizable glucose analogue and inhibitor of phosphohexose isomerase that inhibits glycolysis and mimics glucose starvation, increases the AMP/ATP ratio and thereby activates AMPK.

Antibodies for Pdlim5 and pS177 of Pdlim5. Six polyclonal Pdlim5 antibodies (1:1,000 for immunoblotting and immunostaining) and two polyclonal phospho-Ser177 (pS177)-Pdlim5 antibodies (1:1,000 for immunoblotting) were generated as follows. Three different peptides corresponding to mouse Pdlim5 sequences (amino acids 229–245, QGDIKQQNGPPRKHIVEC; amino acids 290–306, CTGTEHLTESENDNTKKA; and amino acids 381–397, SSGTGASVGPPQPSDQDC), as well as Ser-phosphorylated and non-phosphorylated peptides corresponding to the mouse Pdlim5 sequences surrounding Ser177 (amino acids 172–182, LHLSA(pS)GLHVS), were chemically synthesized. Rabbits were immunized five times with the keyhole limpet haemocyanin–phosphopeptide conjugates mixed with Freund's complete adjuvant and bled 7 days after the last immunization. Phosphopeptide-reactive antibody was captured by a column containing phosphopeptide-conjugated Sepharose. The antibodies were then eluted, and those reactive to sequences other than phosphoserine were removed using a column containing non-phosphorylated peptides. Specific reactivity with the targeted phosphoserine sequence was confirmed by ELISA using phosphorylated and non-phosphorylated peptides.

Cell culture and siRNA transfection. C2C12 cells (an immortalized mouse myoblast cell line) and HEK293T cells were obtained from the American Type Culture Collection. A vSMC line established from thoracic aorta of a p53-knockout mice (P53LMACO1) was purchased from Health Science Research Resources Bank. These cells were maintained in DMEM medium (Sigma-Aldrich) supplemented with 10% FCS (Equitech-Bio) and 1% penicillin–streptomycin at 37 °C in a 5% CO_2 atmosphere at constant humidity and passaged by trypsinization at 70–80% confluence. HL60 cells and RAW264.7 cells were obtained from the Japanese Collection of Research Bioresources Cell Bank and American Type Culture Collection, respectively. These cells were maintained in RPMI1640 medium with 10% FCS and 1% penicillin–streptomycin. HEK293T cells and vSMCs were transfected with plasmids using Lipofectamine 2000 reagent (Invitrogen). To knock down endogenous Pdlim5, C2C12 cells and vSMCs were transfected with siRNAs (30 nM) targeting Pdlim5 (siPdlim5-1, sense: 5′-ggaacaauaugucguggauTT-3′; antisense: 5′-auccacgacauauuguuccTT-3′; siPdlim5-2, sense: 5′-ggguaguagcuaugagaauTT-3′; antisense: 5′-auucucauagcuacuacccTT-3′) using Lipofectamine RNAiMAX (Invitrogen). To knock down endogenous Arpc2, vSMCs were transfected with siRNAs (5 nM) targeting Arpc2 (siArpc2-1, sense: 5′-ggccuauauucauacacgaTT-3′; antisense: 5′-ucguguaugaauauaggccTT-3′; siArpc2-2, sense: 5′-gaaccaggauauauaauguuuTT-3′; antisense: 5′-aaacauuauauaccuggguucTG-3′) using Lipofectamine RNAiMAX (Invitrogen). RAW264.7 cells (mouse leukemic monocyte macrophage cell) were used to check the effect of siRNAs against Arhgef6. RAW264.7 cells were transfected with siRNAs (50 nM) targeting Arhgef6 (siArhgef6-1, sense: 5′-gauucuuaaggugaucgaaTT-3′; antisense: 5′-uucgaucaccuuaagaaucTG-3′; siArhgef6-2, sense: 5′-gugaugaucuagaacgauuTT-3′; antisense: 5′-aaucguucuagaucaucacTG-3′) using GenMute siRNA Transfection Reagent for RAW 264.7 (SignaGen). siControl was used as a negative control. Efficiency of siRNA-mediated knockdown was confirmed at 24 and 72 h after incubation with siRNAs. AMPKα double-knockout ($AMPK\alpha1^{-/-}\alpha2^{-/-}$) MEFs (AMPKα-null MEFs)[25] were kindly provided by Dr B. Viollet (INSERM, France) and maintained in DMEM supplemented with 10% FCS, 1 mM sodium pyruvate and 1% penicillin–streptomycin at 37 °C in a 5% CO_2 atmosphere at constant humidity.

Hypoxia. Cultured cells were exposed to hypoxia for 2 h. Hypoxic conditions (1% O_2) were maintained in a MCO-5M multi-gas incubator (Sanyo).

Establishment of the KDR system. To replace endogenous Pdlim5 by EGFP-tagged recombinant Pdlim5 (WT, S177A or S177D), vSMCs were transfected with siPdlim5-2 to deplete endogenous Pdlim5. Next, 12 h after siPdlim5-2 transfection, siPdlim5-2-resistant EGFP-tagged Pdlim5 (WT, S177A or S177D) was adenovirally transduced into vSMCs, to establish the KDR system. vSMCs were incubated with adenovirus at a multiplicity of infection of 10 in DMEM supplemented with 10% FCS at 37 °C under 5% CO_2 for 30 min, with gentle mixing every 10 min, and then further incubated for 48 h before analysis.

Purification and identification of Pdlim5. C2C12 cells seeded on 15-cm dishes (2×10^6 cells per dish) were treated with 2 mM of AICAR for 1 h, harvested and lysed on ice in lysis buffer A (20 mM Tris pH 8.0, 0.5% NP-40, 0.5% CHAPS, 20% acetonitrile, 25 mM β-glycerophosphate, 10 mM NaF and protease inhibitor cocktail (Nacalai Tesque)). Lysates were incubated at 4 °C with agitation for 20 min, followed by centrifugation at 10,000 *g* for 20 min. Supernatant from six 15-cm dishes was passed through a 0.45-μm sterilization filter and loaded onto a TSK-GEL SuperQ-5PW (7.5 × 75 mm, TOSOH) anion-exchange column pre-equilibrated with column buffer A (20 mM Tris pH 8.0, 0.5% CHAPS, 20% acetonitrile, 25 mM β-glycerophosphate, 10 mM NaF). After being washed with column buffer A, proteins were eluted with a linear gradient of NaCl (0–1 M over 60 min) at a flow rate of 0.5 ml min^{-1}. Fractions (0.5 ml each) were collected and a 50-μl aliquot of each fraction was analysed by immunoblotting with anti-pACC antibody. The corresponding fractions were prepared in the presence of 0.3% TFA (trifluoroacetic acid), 0.1% OG (*n*-octyl-β-D-thioglucopyranoside) and 20% acetonitrile, and loaded onto a Protein-R (4.6 × 250 mm, Nacalai Tesque) reverse-phase HPLC column pre-equilibrated with column buffer B (0.1% TFA and 0.1% OG). After being washed with column buffer B, the proteins were eluted with a linear gradient of acetonitrile (20–80% over 60 min) at a flow rate of 0.5 ml min^{-1}. Fractions (0.5 ml each) were collected and a 25-μl aliquot of each fraction was analysed by immunoblotting with anti-pACC antibody. The corresponding fractions were again prepared in the presence of 0.3% TFA, 0.1% OG and 20% acetonitrile, and loaded onto a 5Ph-AR-300 (4.6 × 250 mm, Nacalai Tesque) reverse-phase HPLC column pre-equilibrated with column buffer B. After being washed with column buffer B, proteins were eluted with a linear gradient of acetonitrile (20–80% over 60 min) at a flow rate of 0.5 ml min^{-1}. Each fraction was analysed by SDS–PAGE and visualized by silver staining and immunoblotting with anti-pACC antibody. Target bands matching the pACC antibody cross-reacting bands were excised from the gel and analysed using matrix-assisted laser desorption/ionization-quadrupole-time-of-flight-tandem mass spectrometry (MALDI-Qq-TOF MS/MS).

Protein purification. Recombinant FLAG-tagged Pdlim5 proteins were purified as follows: HEK293T cells transfected with pEF-DEST51/cFLAG plasmid encoding WT Pdlim5, S175A Pdlim5 or S177A Pdlim5 were lysed in lysis buffer B (20 mM MOPS pH 7.5, 0.15 M NaCl, 0.5% CHAPS, 1 mM EDTA, 1 mM dithiothreitol (DTT) and protease inhibitor cocktail) and immunoprecipitated with anti-FLAG M2 agarose (Sigma-Aldrich) at 4 °C for 30 min. The beads were washed three times with wash buffer (20 mM MOPS pH 7.5, 0.3 M NaCl, 0.5% CHAPS, 1 mM EDTA, 1 mM DTT and protease inhibitor cocktail) and eluted with elution buffer (20 mM MOPS pH 7.5, 0.3 M NaCl, 0.5% CHAPS, 1 mM DTT and 0.5 mg ml^{-1} FLAG peptide (Sigma-Aldrich)) at 4 °C for 30 min. After centrifugation, the supernatants were used as recombinant FLAG-tagged proteins. Recombinant GST-Pdlim5 proteins (WT, S177A, S177D and ΔPDZ) were purified as follows: BL21 chemically competent *E. coli* (Invitrogen) were transformed with pGEX-6P-1-WT Pdlim5, pGEX-6P-1-S177A Pdlim5, pGEX-6P-1-S177D Pdlim5 or pGEX-6P-1-ΔPDZ Pdlim5, and then induced with 0.5 mM isopropyl-β-D-thiogalactoside (Sigma-Aldrich) at 25 °C for 10 h. The cells were collected by centrifugation and lysed by sonication in PBS containing 5 mM EDTA and protease inhibitor cocktail. After addition of 1% Triton X-100, the lysates were agitated at 4 °C for 30 min and pulled down with glutathione–Sepharose 4 Fast Flow (GE Healthcare) at 4 °C for 1 h. After being washed three times, the proteins were eluted with 15 mM reduced glutathione and ultrafiltered in elution buffer using a Nanosep 10K Device (Pall Life Science).

Immunoblotting. Immunoblotting was performed using the indicated antibodies. Blots were cropped such that at least one marker position is present. Uncropped full scans of the figures are supplied in Supplementary Figs 17–23.

Phosphorylation assay. Phosphorylation assays were carried out at 30 °C in a reaction volume of 10 μl containing Tris-HCl (20 mM pH 7.4), glycerol (10%), NaCl (0.3 mM), AMP (0.2 mM), MgCl2 (10 mM), γ-^{32}P ATP (GE Healthcare BioScience, 10 μCi, 1.7 pmol) and AMPK purified from rat liver (2 ng μl^{-1}). Purified mouse Pdlim5-cFLAG proteins or purified recombinant GST-fused mouse Pdlim5 proteins were used as substrates. After 60 min, reactions were terminated and ultrafiltered in PBS containing 0.1% SDS using a Nanosep 10K Device (Pall Life Science). Each fraction sample was analysed by SDS–PAGE and visualized by autoradiography. For immunoblotting with anti-pS177 antibody, recombinant GST-fused Pdlim5 proteins were incubated under the same conditions, except that ATP (0.1 mM) was included instead of γ-^{32}P ATP.

Scratch assay. KDR/EGFP-Pdlim5 (WT, S177A and S177D) cells or MEFs were plated on a collagen-coated 35-mm glass dish at a density of 5×10^5 cm^{-2}. Eight hours after plating, a scratch was made with a P-200 pipette tip and the lesions were observed for a total of 8 h. Differential interference contrast images were

recorded every 5 min using an Olympus LCV110 incubator microscope (Olympus Corporation, Tokyo, Japan). To determine cell trajectories, the centrioles of cell nuclei were tracked throughout time-lapse movies, and migration-tracking images were generated using the MetaMorph 7.1.3.0 software (MDS Analytical Technologies, Downingtown, PA, USA). Overall migration speed was calculated as the average of migration speeds measured every 5 min.

Single-cell migration assay. KDR/EGFP-Pdlim5 (WT, S177A and S177D) cells were plated on a collagen-coated 35-mm glass dish at a density of 5×10^5 cm^{-2}. Five hours after the plating, we started to observe cell migration by recording differential interference contrast images every 5 min for a total of 4 h using an Olympus LCV110 incubator microscope (Olympus Corporation).

Immunocytochemistry and fluorescence imaging. vSMCs or KDR cells were seeded on a collagen-coated 35-mm glass dishes (Asahi Techno Glass Corporation, Chiba, Japan). After cells firmly attached to the dish, they were washed once with warm PBS and fixed with 4% paraformaldehyde for 5 min at room temperature. Next, the cells were permeabilized with 0.1% Triton X-100 in PBS for 5 min at room temperature and then blocked with 1% BSA at 4 °C overnight. The next day, samples were immunostained with primary antibodies (1:1,000 in 1% BSA, 1 h). For secondary reactions, species-matched Alexa Fluor 488- or Alexa Fluor 568-labelled secondary antibody was used (1:1,000 in 1% BSA, 30 min). Just before imaging, the sample was incubated with Alexa Fluor 647-conjugated phalloidin in CGS-Sol A for 1 h. Fluorescence images of EGFP, Alexa Fluor 488, Alexa Fluor 546, Alexa Fluor 568 and Alexa Fluor 647 were recorded using an Olympus FV1000-D confocal laser scanning microscope (Olympus Corporation) equipped with a cooled charge-coupled device CoolSNAP-HQ camera (Roper Scientific, Tucson, AZ, USA) and a PLAPO ×60 oil-immersion objective lens. To measure the paxillin-positive area, all intensity profiles were analysed using the MetaMorph 7.1.3.0 software.

Time-lapse imaging of KDR/EGFP-Pdlim5 cells. KDR/EGFP-Pdlim5 (WT and S177A) cells were seeded on collagen-coated 35-mm glass dishes at a density of 4×10^4 cm^{-2}. Five hours after plating, cells were treated with AICAR (2 mM). The fluorescence images were recorded from 10 min before to 60 min after AICAR treatment, using an Olympus IX-81 inverted fluorescence microscope (Olympus Corporation) equipped with a cooled charge-coupled device CoolSNAP-HQ camera (Roper Scientific) and a PLAPO ×60 oil-immersion objective lens controlled by MetaMorph version 7.1.3.0. An EGFP image was obtained every 30 s through a U-MNIBA2 filter (Olympus Corporation), which had a 470–495 excitation filter and a 510–550 emission filter. Cells were maintained on a microscope at 37 °C with a 5% carbon dioxide mixture using a stage-top incubator (Tokai Hit). MetaMorph was used to convert a series of time-lapse images to video format.

Measurement of the GTP-bound form of Rac1, RhoA and Cdc42. KDR cells at 50%confluence were incubated for 24 h in FCS-free DMEM to starve the cells, and then treated with 10% FCS for 30 min. Cell lysates were collected and levels of activated GTP-bound Rac1, RhoA and Cdc42 were determined using the G-LISA Rac1 Activation Assay Biochem Kit (BK126, Cytoskeleton Inc., CO, USA), G-LISA RhoA Activation Assay Biochem Kit (BK121, Cytoskeleton Inc.) and G-LISA Cdc42 Activation Assay Biochem Kit (BK127, Cytoskeleton Inc.), respectively.

Imaging of Rho GTPases (Rac1, RhoA and Cdc42) activities. To visualize activities of Rho GTPases in living cells, we established a vSMC cell line stably expressing a Rho GTPase FRET biosensor consisting of cyan fluorescent protein (CFP) and yellow fluorescent protein (YFP), as previously described[43]. In brief, vSMCs were transfected with the CFP/YFP-type FRET biosensor gene for Rho GTPases, using the PiggyBac retrotransposon-mediated gene transfer system, and then cultured for 2 w with 10 μg ml^{-1} blasticidin S to select for vSMCs stably expressing the FRET biosensor (Raichu-Rac1, RhoA or Cdc42/vSMC). Next, a KDR system for vSMCs expressing Raichu-Rac1, Raichu-RhoA or Rhaicu-Cdc42 was established as described above, except for the use of an adenovirus encoding non-tagged Pdlim5 (WT, S177A and S177D)-T2A-mCherry instead of EGFP-tagged Pdlim5 (Raichu-Rac1, RhoA or Cdc42/KDR-Pdlim5-T2A-mCherry). Forty-eight hours after the transduction of Pdlim5-T2A-mCherry, Raichu-Rac1, RhoA or Cdc42/KDR-Pdlim5-T2A-mCherry cells were re-plated on collagen-coated glass-base dishes. All experiments were performed at 37 °C in a 5% CO_2 atmosphere using a heating chamber. Dual images for CFP and YFP were obtained on a laser scanning microscope (LSM710, Zeiss) using an excitation wavelength of 405 nm and emission bandpass filters of 458–510 nm for CFP and 517–598 nm for YFP. After background subtraction, FRET/CFP ratio images were created using the LSM software ZEN2011 (Zeiss) and displayed as an intensity-modulated display image. For quantitative FRET analysis, the FRET/CFP ratio of each cell was calculated by dividing the fluorescence intensity of YFP by that of CFP over the total cellular area.

GST pull-down assay. For identification of proteins associated with Pdlim5, 20 μg of purified GST-tagged Pdlim5 WT or S177D-Pdlim5 was immobilized on glutathione–Sepharose beads and incubated at 4 °C for 2 h with cell lysate from 2×10^9 U937 cells in lysis buffer (30 mM MOPS pH 7.5, 150 mM NaCl, 0.5% Triton-X100, 1.5 mM $MgCl_2$, 1 mM EGTA, 1 mM DTT and protease inhibitor cocktail). After three washes of the beads with lysis buffer, associated proteins were eluted in elution buffer (30 mM MOPS pH 7.5, 500 mM NaCl, 0.5% Triton-X100, 1.5 mM $MgCl_2$, 1 mM EGTA, 1 mM DTT and protease inhibitor cocktail) and then subjected to silver staining and high-sensitivity shotgun liquid chromatography–mass spectrometry (LTQ Orbitrap ELITE, Thermo Scientific).

F-actin binding assay of AMPK. F-actin binding assays were performed using the Actin Binding Protein Biochem Kit (BK001, Cytoskeleton, Inc.) according to the manufacturer's protocol, with minor modifications. Briefly, 1 μl of F-actin (21 μM actin) in actin polymerization buffer (100 mM KCl, 2 mM $MgCl_2$, 0.5 mM ATP, 0.2 mM Tris-HCl, pH 8.0) was mixed with 0.5 μl of purified AMPK (200 ng μl^{-1}) in the presence or absence of GST-tagged WT-Pdlim5 and 1 μl of α-actinin (1 μg μl^{-1}) in 60 μl reaction volume, incubated for 1 h at 24 °C and then centrifuged at 150,000 *g* for 1.5 h at 24 °C, to pellet the F-actin polymer and associated proteins. Equal amounts of pellet (P) and supernatant (S) were resolved by SDS–PAGE and analysed by immunoblotting with the indicated antibodies.

Statistical analyses. Box plots show the entire population. Other data are expressed as means ± s.e.m. Two-tailed Student's *t*-test was used to analyse differences between two groups. Differences among multiple groups were compared by one-way analysis of variance, followed by a *post-hoc* comparison with Dunnett's method using the JMP 8.0.1 software (SAS Institute Inc., Cary, NC, USA). $P < 0.01$ was considered to indicate statistically significant differences.

References

1. Carling, D., Mayer, F. V., Sanders, M. J. & Gamblin, S. J. AMP-activated protein kinase: nature's energy sensor. *Nat. Chem. Biol.* **7,** 512–518 (2011).
2. Lee, J. H. *et al.* Energy-dependent regulation of cell structure by AMP-activated protein kinase. *Nature* **447,** 1017–1020 (2007).
3. Zhang, L., Li, J., Young, L. H. & Caplan, M. J. AMP-activated protein kinase regulates the assembly of epithelial tight junctions. *Proc. Natl Acad. Sci. USA* **103,** 17272–17277 (2006).
4. Nakano, A. *et al.* AMPK controls the speed of microtubule polymerization and directional cell migration through CLIP-170 phosphorylation. *Nat. Cell Biol.* **12,** 583–590 (2010).
5. Bae, H. B. *et al.* AMP-activated protein kinase enhances the phagocytic ability of macrophages and neutrophils. *FASEB J.* **25,** 4358–4368 (2011).
6. Kondratowicz, A. S., Hunt, C. L., Davey, R. A., Cherry, S. & Maury, W. J. AMP-activated protein kinase is required for the macropinocytic internalization of ebolavirus. *J. Virol.* **87,** 746–755 (2013).
7. Parsons, J. T., Horwitz, A. R. & Schwartz, M. A. Cell adhesion: integrating cytoskeletal dynamics and cellular tension. *Nat. Rev. Mol. Cell Biol.* **11,** 633–643 (2010).
8. Wu, Y. I. *et al.* A genetically encoded photoactivatable Rac controls the motility of living cells. *Nature* **461,** 104–108 (2009).
9. Sanz-Moreno, V. *et al.* Rac activation and inactivation control plasticity of tumor cell movement. *Cell* **135,** 510–523 (2008).
10. Campellone, K. G. & Welch, M. D. A nucleator arms race: cellular control of actin assembly. *Nat. Rev. Mol. Cell Biol.* **11,** 237–251 (2010).
11. Ridley, A. J. Life at the leading edge. *Cell* **145,** 1012–1022 (2011).
12. Dihu, J. B., Abudayyeh, I., Saudye, H. A. & Gurujal, R. Cilostazol: a potential therapeutic option to prevent in-stent restenosis. *J. Am. Coll. Cardiol.* **57,** 2035–2036 (2011).
13. Nissen, S. E. *et al.* Comparison of pioglitazone vs glimepiride on progression of coronary atherosclerosis in patients with type 2 diabetes: the PERISCOPE randomized controlled trial. *JAMA* **299,** 1561–1573 (2008).
14. Bailey, C. J. Metformin: effects on micro and macrovascular complications in type 2 diabetes. *Cardiovasc. Drugs Ther.* **22,** 215–224 (2008).
15. Esfahanian, N. *et al.* Effect of metformin on the proliferation, migration, and MMP-2 and -9 expression of human umbilical vein endothelial cells. *Mol. Med. Rep.* **5,** 1068–1074 (2012).
16. Ridley, A. J. *et al.* Cell migration: integrating signals from front to back. *Science* **302,** 1704–1709 (2003).
17. Gruzman, A., Babai, G. & Sasson, S. Adenosine monophosphate-activated protein kinase (AMPK) as a new target for antidiabetic drugs: a review on metabolic, pharmacological and chemical considerations. *Rev. Diabetic Studies* **6,** 13–36 (2009).
18. te Velthuis, A. J. & Bagowski, C. P. PDZ and LIM domain-encoding genes: molecular interactions and their role in development. *Sci. World J.* **7,** 1470–1492 (2007).
19. Zheng, Q. & Zhao, Y. The diverse biofunctions of LIM domain proteins: determined by subcellular localization and protein-protein interaction. *Biol. Cell* **99,** 489–502 (2007).

20. Lasorella, A. & Iavarone, A. The protein ENH is a cytoplasmic sequestration factor for Id2 in normal and tumor cells from the nervous system. *Proc. Natl Acad. Sci. USA* **103,** 4976–4981 (2006).
21. Yoshizaki, H. *et al.* Activity of Rho-family GTPases during cell division as visualized with FRET-based probes. *J. Cell Biol.* **162,** 223–232 (2003).
22. Feng, Q., Baird, D. & Cerione, R. A. Novel regulatory mechanisms for the Dbl family guanine nucleotide exchange factor Cool-2/alpha-Pix. *EMBO J.* **23,** 3492–3504 (2004).
23. Matsuda, C. *et al.* Affixin activates Rac1 via betaPIX in C2C12 myoblast. *FEBS Lett.* **582,** 1189–1196 (2008).
24. Viollet, B. *et al.* AMPK: Lessons from transgenic and knockout animals. *Front. Biosci. (Landmark Ed)* **14,** 19–44 (2009).
25. Laderoute, K. R. *et al.* 5′-AMP-activated protein kinase (AMPK) is induced by low-oxygen and glucose deprivation conditions found in solid-tumor microenvironments. *Mol. Cell Biol.* **26,** 5336–5347 (2006).
26. Faubert, B. *et al.* AMPK is a negative regulator of the Warburg effect and suppresses tumor growth in vivo. *Cell Metab.* **17,** 113–124 (2013).
27. Cheng, H. *et al.* Loss of enigma homolog protein results in dilated cardiomyopathy. *Circ. Res.* **107,** 348–356 (2010).
28. Horiuchi, Y. *et al.* Experimental evidence for the involvement of PDLIM5 in mood disorders in hetero knockout mice. *PLoS ONE* **8,** e59320 (2013).
29. Rosenberger, G., Jantke, I., Gal, A. & Kutsche, K. Interaction of alphaPIX (ARHGEF6) with beta-parvin (PARVB) suggests an involvement of alphaPIX in integrin-mediated signaling. *Hum. Mol. Genet.* **12,** 155–167 (2003).
30. Mishima, W. *et al.* The first CH domain of affixin activates Cdc42 and Rac1 through alphaPIX, a Cdc42/Rac1-specific guanine nucleotide exchanging factor. *Genes Cells* **9,** 193–204 (2004).
31. Cabodi, S., del Pilar Camacho-Leal, M., Di Stefano, P. & Defilippi, P. Integrin signalling adaptors: not only figurants in the cancer story. *Nat. Rev. Cancer* **10,** 858–870 (2010).
32. Wickstrom, S. A., Lange, A., Montanez, E. & Fassler, R. The ILK/PINCH/parvin complex: the kinase is dead, long live the pseudokinase! *EMBO J.* **29,** 281–291 (2010).
33. Yamaji, S. *et al.* Affixin interacts with alpha-actinin and mediates integrin signaling for reorganization of F-actin induced by initial cell-substrate interaction. *J. Cell Biol.* **165,** 539–551 (2004).
34. Nakagawa, N. *et al.* ENH, containing PDZ and LIM domains, heart/skeletal muscle-specific protein, associates with cytoskeletal proteins through the PDZ domain. *Biochem. Biophys. Res. Commun.* **272,** 505–512 (2000).
35. Michaelson, D. *et al.* Differential localization of Rho GTPases in live cells: regulation by hypervariable regions and RhoGDI binding. *J. Cell Biol.* **152,** 111–126 (2001).
36. Johnston, S. A., Bramble, J. P., Yeung, C. L., Mendes, P. M. & Machesky, L. M. Arp2/3 complex activity in filopodia of spreading cells. *BMC Cell Biol.* **9,** 65 (2008).
37. Suraneni, P. *et al.* The Arp2/3 complex is required for lamellipodia extension and directional fibroblast cell migration. *J. Cell Biol.* **197,** 239–251 (2012).
38. Wu, C. *et al.* Arp2/3 is critical for lamellipodia and response to extracellular matrix cues but is dispensable for chemotaxis. *Cell* **148,** 973–987 (2012).
39. Hotulainen, P. & Lappalainen, P. Stress fibers are generated by two distinct actin assembly mechanisms in motile cells. *J. Cell Biol.* **173,** 383–394 (2006).
40. Sander, E. E., ten Klooster, J. P., van Delft, S., van der Kammen, R. A. & Collard, J. G. Rac downregulates Rho activity: reciprocal balance between both GTPases determines cellular morphology and migratory behavior. *J. Cell Biol.* **147,** 1009–1022 (1999).
41. Chauhan, B. K., Lou, M., Zheng, Y. & Lang, R. A. Balanced Rac1 and RhoA activities regulate cell shape and drive invagination morphogenesis in epithelia. *Proc. Natl Acad. Sci. USA* **108,** 18289–18294 (2011).
42. Kovar, D. R., Harris, E. S., Mahaffy, R., Higgs, H. N. & Pollard, T. D. Control of the assembly of ATP- and ADP-actin by formins and profilin. *Cell* **124,** 423–435 (2006).
43. Aoki, K., Komatsu, N., Hirata, E., Kamioka, Y. & Matsuda, M. Stable expression of FRET biosensors: a new light in cancer research. *Cancer Sci.* **103,** 614–619 (2012).

Acknowledgements

This research was supported by the Japan Society for the Promotion of Science (JSPS) through the Funding Program for Next-Generation World-Leading Researchers (NEXT Program), which was initiated by the Council for Science and Technology Policy (CSTP); grants-in-aid from the Ministry of Health, Labour and Welfare of Japan; grants-in-aid from the Ministry of Education, Culture, Sports, Science and Technology of Japan; and grants-in-aid from the Japan Society for the Promotion of Science. This research was also supported by grants from the Japan Heart Foundation, the Japan Cardiovascular Research Foundation, the Japan Medical Association, the Japan Intractable Diseases Research Foundation, the Uehara Memorial Foundation, the Takeda Science Foundation, the Ichiro Kanehara Foundation, the Inoue Foundation for Science, the Mochida Memorial Foundation, a Heart Foundation/Novartis Grant for Research Award on Molecular and Cellular Cardiology, the Japan Foundation of Applied Enzymology, the Naito Foundation, the Banyu Foundation and Showa Houkoukai. We thank Hitoshi Miyagi, Kenichi Kondo (Olympus Corporation) and Masako Yamaguchi (Carl Zeiss Microscopy Corporation) for technical advice regarding microscopy; Saori Ikezawa, Eri Takata and Keiko Singu for technical assistance; and Yuko Okada for secretarial support.

Authors contributions

Y.Y. and O.T. designed and conducted the study, performed most of the experiments and wrote the manuscript. S.T. designed and wrote the manuscript. A.N. discussed the results and helped to write the manuscript. H.K. and K.T. performed the proteomic analysis. H.K. conducted and supported the biological experiments. N.I. performed the biochemical experiments and helped to generate plasmids. S.H., S.Y., Y.S., K.M. and Y.A. discussed the results and reviewed the manuscript. Y.L. H.A., M.A. and T.M. discussed the results. M.K. supervised all work.

Additional information

Supplementary Information accompanies this paper at http://www.nature.com/naturecommunications

Competing financial interests: The authors declare no competing financial interests.

Reprints and permission information is available online at http://npg.nature.com/reprintsandpermissions/

How to cite this article: Yan, Y. *et al.* Augmented AMPK activity inhibits cell migration by phosphorylating the novel substrate Pdlim5. *Nat. Commun.* 6:6137 doi: 10.1038/ncomms7137 (2015).

Higd1a is a positive regulator of cytochrome *c* oxidase

Takaharu Hayashi[a,b], Yoshihiro Asano[a,b,1], Yasunori Shintani[a], Hiroshi Aoyama[c], Hidetaka Kioka[b], Osamu Tsukamoto[a], Masahide Hikita[d], Kyoko Shinzawa-Itoh[d], Kazuaki Takafuji[e], Shuichiro Higo[a,b], Hisakazu Kato[a], Satoru Yamazaki[f], Ken Matsuoka[b], Atsushi Nakano[g], Hiroshi Asanuma[h], Masanori Asakura[g], Tetsuo Minamino[b], Yu-ichi Goto[i], Takashi Ogura[d], Masafumi Kitakaze[g], Issei Komuro[j], Yasushi Sakata[b], Tomitake Tsukihara[d,k], Shinya Yoshikawa[d], and Seiji Takashima[a,k,1]

Departments of [a]Medical Biochemistry and [b]Cardiovascular Medicine, [e]Center for Research Education, and [c]Graduate School of Pharmaceutical Science, Osaka University Graduate School of Medicine, Suita, Osaka 565-0871, Japan; [d]Department of Life Science, University of Hyogo, 3-2-1 Kouto, Kamigohri, Akoh, Hyogo 678-1297, Japan; [k]Core Research for Evolutional Science and Technology (CREST), Japan Science and Technology Agency, Kawaguchi, Saitama 332-0012, Japan; Departments of [f]Cell Biology and [g]Clinical Research and Development, National Cerebral and Cardiovascular Center Research Institute, Suita, Osaka 565-8565, Japan; [h]Department of Cardiovascular Science and Technology, Kyoto Prefectural University School of Medicine, Kamigyo-ku, Kyoto 602-8566, Japan; [i]Department of Child Neurology, National Center Hospital of Neurology and Psychiatry, National Center of Neurology and Psychiatry, Kodaira, Tokyo 187-8502, Japan; and [j]Department of Cardiovascular Medicine, Graduate School of Medicine, University of Tokyo, Tokyo 113-8656, Japan

Edited by Gottfried Schatz, University of Basel, Reinach, Switzerland, and approved December 16, 2014 (received for review October 15, 2014)

Cytochrome *c* oxidase (CcO) is the only enzyme that uses oxygen to produce a proton gradient for ATP production during mitochondrial oxidative phosphorylation. Although CcO activity increases in response to hypoxia, the underlying regulatory mechanism remains elusive. By screening for hypoxia-inducible genes in cardiomyocytes, we identified *hypoxia inducible domain family, member 1A* (*Higd1a*) as a positive regulator of CcO. Recombinant Higd1a directly integrated into highly purified CcO and increased its activity. Resonance Raman analysis revealed that Higd1a caused structural changes around heme *a*, the active center that drives the proton pump. Using a mitochondria-targeted ATP biosensor, we showed that knockdown of endogenous Higd1a reduced oxygen consumption and subsequent mitochondrial ATP synthesis, leading to increased cell death in response to hypoxia; all of these phenotypes were rescued by exogenous Higd1a. These results suggest that Higd1a is a previously unidentified regulatory component of CcO, and represents a therapeutic target for diseases associated with reduced CcO activity.

cytochrome *c* oxidase | oxidative phosphorylation | resonance Raman spectroscopy | ATP | oxygen

Cytochrome *c* oxidase (CcO) (ferrocytochrome c: oxygen oxidoreductase, EC 1. 9. 3. 1) is the terminal component of the mitochondrial electron transfer system. CcO couples the oxygen-reducing reaction with the process of proton pumping. Aerobic organisms use this reaction to form a proton gradient across the mitochondrial inner membrane, which is ultimately used by the F_oF_1-ATP synthase to produce ATP.

Mammalian CcO is composed of 13 different subunits (1) containing four redox-active metal centers, two copper sites, and two heme *a* groups. These active centers accept electrons from cytochrome *c* and sequentially donate them to dioxygen. Our group and others have extensively analyzed the link between the oxygen reduction process and proton pumping at the active centers using crystallography, resonance Raman spectroscopy, and Fourier transform infrared spectroscopy (2–4). The metal ions in the copper sites and heme groups in the active centers are individually coordinated by the surrounding amino acids. We have shown that changes in the redox state cause 3D structural changes around the active centers, which in turn leads to alteration of the proton pump mediated by specific amino acid chains that coordinate each metal group (5). Thus, binding of an allosteric regulator close to the active centers might change the efficiency of both electron transfer to oxygen and proton pumping.

Several proteins involved in oxygen supply or metabolism are transcriptionally regulated by intracellular oxygen concentration: vascular endothelial growth factor (VEGF) (6), erythropoietin (EPO) (7), and G0/G1 switch gene 2 (G0s2) for F_oF_1-ATP synthase, as we recently revealed (8). Because CcO is the only enzyme in the body that can use oxygen for energy transduction, it has been suggested that the regulatory mechanism of CcO is dependent on oxygen concentration (9–12); however, this has yet to be demonstrated. In this study, we aimed to identify a regulator of CcO driven by low oxygen concentration.

In this study, by screening for hypoxia-inducible genes, we discovered that *hypoxia inducible domain family, member 1A (Higd1a)* is a positive regulator of CcO. Furthermore, using our recently established ATP-sensitive fluorescence resonance energy transfer (FRET) probe, we demonstrated that Higd1a increased mitochondrial ATP production. We also showed that Higd1a directly bound CcO and changed the structure of its active center.

Results

***Higd1a* Expression Is Induced Early in the Response to Hypoxia.** During the first few hours of hypoxia, CcO and oxidative phosphorylation (OXPHOS) activity is activated, presumably to fully use any remaining oxygen (12). At later time points, metabolism shifts toward glycolysis. Therefore, we hypothesized that a positive regulator of CcO must be up-regulated during an early stage of hypoxia, but down-regulated when glycolysis-related genes become elevated. To identify early hypoxia responsive genes that

Significance

We identified hypoxia-inducible domain family, member 1A (Higd1a) as a positive regulator of cytochrome *c* oxidase (CcO). CcO, the terminal component of the mitochondrial electron transfer system, reductively converts molecular oxygen to water coupled to pump protons across the inner mitochondrial membrane. Higd1a is transiently induced under hypoxic conditions and increases CcO activity by directly interacting with CcO in the vicinity of its active center. Induction of Higd1a leads to increased oxygen consumption and subsequent mitochondrial ATP synthesis, thereby improving cell viability under hypoxia.

Author contributions: Y.A., Y. Shintani, H. Kioka, T.T., S. Yoshikawa, and S.T. designed research; T.H., Y. Shintani, H. Kioka, O.T., M.H., K.S.-I., K.T., and H. Kato performed research; H. Aoyama, M.H., Y.-i.G., T.O., M.K., I.K., Y. Sakata, T.T., and S. Yoshikawa contributed new reagents/analytic tools; T.H., Y. Shintani, S.H., S. Yamazaki, K.M., A.N., H. Asanuma, M.A., and T.M. analyzed data; and T.H., Y. Shintani, H. Kato, T.O., T.T., S. Yoshikawa, and S.T. wrote the paper.

The authors declare no conflict of interest.

This article is a PNAS Direct Submission.

[1]To whom correspondence may be addressed. Email: takasima@cardiology.med.osaka-u.ac.jp or asano@cardiology.med.osaka-u.ac.jp.

This article contains supporting information online at www.pnas.org/lookup/suppl/doi:10.1073/pnas.1419767112/-/DCSupplemental.

might regulate CcO activity, we analyzed gene-expression profiles of neonatal rat cardiomyocytes, one of the most mitochondria-rich cell types, exposed to hypoxic conditions (1% oxygen for 0, 4, or 12 h). Focusing on the genes whose expression was induced more than two-fold at 4 h relative to the prestimulation stage, but then decreased by 12 h, we identified three genes (Fig. 1*A* and Fig. S1 *A* and *B*). Next, we prioritized genes that were (*i*) well conserved among eukaryotes and (*ii*) listed in MitoCarta (13); only one gene, *Higd1a*, satisfied both criteria. To analyze the endogenous expression levels of Higd1a in rat cardiomyocytes, we raised a specific antibody against Higd1a and confirmed its specificity (Fig. S2 *A* and *B*). In cardiomyocytes exposed to hypoxia, Higd1a protein levels increased gradually from 0 to 12 h and then decreased by 24 h (Fig. 1*B*). Immunofluorescence revealed that both endogenous and exogenous Higd1a localized in the mitochondria (Fig. S2*C*).

Higd1a Directly Integrates into the CcO Macromolecular Complex. Because Rcf1a, the yeast homolog of Higd1a, associates with CcO (9–11), we first tested whether mammalian Higd1a binds to CcO in vivo. Indeed, endogenous binding between Higd1a and CcO in rat cardiomyocytes was confirmed by immunocapture with an anti-Higd1a antibody (Fig. S3*A*) and verified by reciprocal coimmunoprecipitation with an anti-Cox4 antibody (Fig. S3*B*). This in vivo interaction was further validated by blue native PAGE (BN-PAGE) of mitochondrial fractions from rat cardiomyocytes (Fig. S3*C*).

Because preparation of the CcO macromolecular complex, which consists of 13 subunits, is technically demanding, it has remained unclear whether Rcf1a/Higd1a binding to CcO is direct. To address this issue, we performed an in vitro pull-down assay using highly purified bovine CcO (hpCcO), which we prepared by dissolving microcrystals used for X-ray structural analysis (14). Notably, recombinant maltose binding protein-fused bovine Higd1a (MBP-Higd1a) (Fig. S4) directly associated with hpCcO (Fig. 1*C*). Furthermore, to assess macromolecular complex formation, we performed BN-PAGE followed by immunoblotting with an antibody against Higd1a, demonstrating that recombinant Higd1a indeed integrated into hpCcO (Fig. 1*D*). With these results, we conclude that Higd1a directly associates and integrates into the CcO macromolecular complex.

Higd1a Causes Structural Changes in CcO and Influences the Active Center of Heme *a*. To explore the relevance of the interaction between Higd1a and CcO, we investigated whether recombinant Higd1a affects hpCcO enzymatic activity. Strikingly, direct addition of MBP-Higd1a to hpCcO significantly increased CcO activity to twice that of hpCcO alone or hpCcO mixed with MBP (Fig. 2*A*). This significant increase in hpCcO activity stimulated by Higd1a led us to speculate that Higd1a causes a structural change at the active centers of CcO.

Therefore, we next investigated whether Higd1a changes the intensity of the visible part of the absorption spectrum of oxidized CcO. MBP alone, used as a negative control, did not cause a significant change in the absorption spectra (Fig. S5). By contrast, MBP-Higd1a caused significant spectral changes at 413 nm and 432 nm (Fig. 2*B*), wavelengths that reflect conformational changes around the hemes in oxidized CcO (15).

To obtain further structural insights, we performed resonance Raman spectroscopy, a powerful and sensitive method for detecting kinetic structural changes that cannot be assessed by X-ray crystal structural analysis. Fig. 2*C* depicts the resonance Raman spectra of CcO with and without MBP-Higd1a, focusing on the heme structure by using 413 nm excitation. The resonance Raman band at 1,372 cm^{-1} in (a: hpCcO) and (b: hpCcO + Higd1a) is assignable to the ν_4 mode of heme and is indicative of ferric heme. After the addition of recombinant Higd1a, the resonance Raman spectra demonstrated two sets of different peaks (or band shifts) at 1,562/1,592 cm^{-1} (the ν_2 mode; a marker for the spin state of heme) (16) and 1,673/1,644 cm^{-1} (the $\nu_{CH=O}$ mode of the formyl group of heme *a*) (17). Importantly, the frequency shift of the band at 1,592 cm^{-1} to 1,562 cm^{-1} is attributable to partial conversion of heme from a low-spin to a high-spin state. In oxidized CcO, only heme *a* includes low-spin iron; therefore, heme *a*, but not heme a_3, is responsible for the band shift (16). These data suggest that the binding of Hig1a to CcO caused structural changes at heme *a*, the active center of CcO.

Higd1a Positively Regulates CcO Activity and Subsequent Mitochondrial OXPHOS. Next, we investigated whether Higd1a truly regulates CcO activity in vivo. To this end, we assessed biochemical CcO activity in rat cardiomyocytes with modified expression of Higd1a. Notably, we observed a significant decrease in CcO activity in Higd1a knockdown cells. This effect was rescued by overexpression of Higd1a, eliminating the possibility of off-target effects in the RNAi experiment (Fig. 3*A*, *Left*). Moreover, overexpression of Higd1a alone increased the basal CcO activity (Fig. 3*A*, *Right*). These data suggest that Higd1a is an endogenous and positive regulator of CcO.

To assess the effect of Higd1a on cellular respiration, we continuously measured the oxygen consumption rate (OCR) using a XF96 Extracellular Flux Analyzer (Seahorse Bioscience).

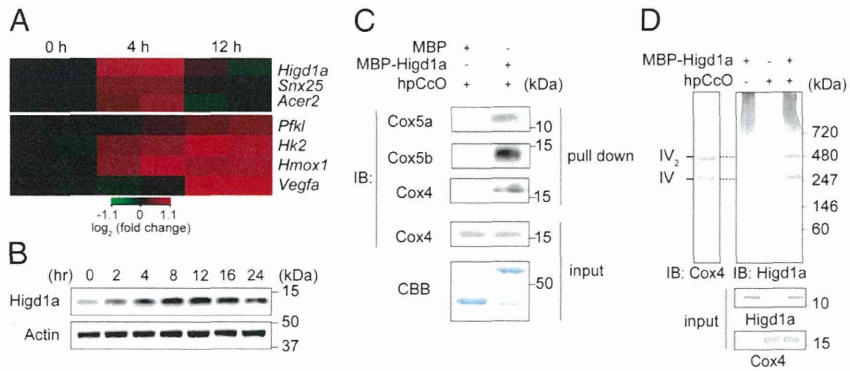

Fig. 1. Hypoxia-inducible Higd1a directly binds to highly purified cytochrome *c* oxidase (hpCcO). (*A*) Heat map of three genes (*Upper*) identified as relatively rapid and transiently induced in response to hypoxia in rat neonatal cardiomyocytes, compared with genes known to be hypoxia inducible (*Pfkl*, *Hk2*, *Hmox1*, and *Vegfa*) (*Lower*). (*B*) Expression of the Higd1a protein was elevated in response to hypoxia. (*C*) In vitro pull-down assay with amylose resin revealed direct binding between MBP-Higd1a and the hpCcO from bovine heart. Loading controls for the hpCcO and MBP-fusion proteins are shown in immunoblots for anti-CcO subunits and CBB staining, respectively. (*D*) MBP-Higd1a directly integrates into hpCcO. Mixed MBP-fusion proteins and hpCcO containing 0.2% *n*-decyl-β-D-maltoside (DM) were resolved by blue native PAGE (BN-PAGE), followed by immunoblotting with anti-Cox4 to detect CcO and anti-Higd1a to detect Higd1a.

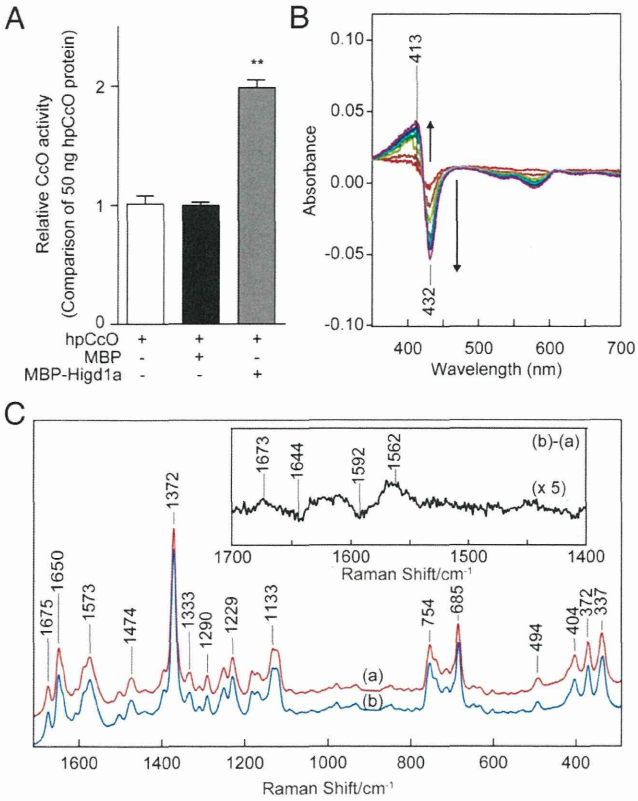

Fig. 2. Higd1a regulates CcO activity through the structural change of the active center in CcO. (*A*) CcO activity of hpCcO and hpCcO with either recombinant MBP or recombinant MBP-Higd1a. MBP-Higd1a causes an increase in CcO activity by almost twofold. Data represent the means ± SEM of five individual experiments. $^{**}P < 0.01$, compared with MBP. (*B*) The difference in absorption spectra between MBP-Higd1a and oxidized hpCcO. MBP-Higd1a caused spectral changes at 413 and 432 nm. Intensity changes of oxidized hpCcO spectra are plotted at 1 min (red), 5 min (brown), 10 min (dark yellow), 15 min (green), 20 min (light blue), 25 min (blue), and 30 min (purple) after adding MPB-Higd1a. (*C*) Resonance Raman spectra of oxidized hpCcO at 0–5 min [spectrum (a)] and oxidized hpCcO mixed with MBP-Higd1a at 0–5 min [spectrum (b)]. The *Inset* shows the difference of the spectra [(b) − (a)].

Knockdown of Higd1a caused a significant decrease in both basal (Fig. S6*A*, *Left*) and maximum OCR, and these effects were rescued by exogenous expression of Higd1a (Fig. 3*B*, *Left*). Moreover, overexpression of Higd1a significantly increased both basal and maximum OCR (Fig. S6*A*, *Right* and Fig. 3*B*, *Right*).

Because the electron transport chain creates a proton gradient that drives F_oF_1-ATP synthase (complex V), ATP production is the overall outcome of mitochondrial OXPHOS. To determine whether modulation of CcO activity by Higd1a affects ATP production, we performed the mitochondrial activity of streptolysin O permeabilized cells (MASC) assay, a sensitive means of measuring the mitochondrial ATP production rate in semi-intact cells (18). Indeed, Higd1a knockdown caused a significant decrease in the ATP production rate relative to the control (Fig. 3*C*), whereas overexpression of Higd1a increased it (Fig. 3*D*). These results suggest that Higd1a modulates mitochondrial OXPHOS through CcO.

Higd1a Protects Cardiomyocytes Under Hypoxic Conditions by Increasing ATP Production. We reasoned that endogenous induction of Higd1a by hypoxia serves to maintain ATP production in mitochondria to the greatest extent possible when oxygen supply is limited. The intramitochondrial matrix ATP concentration ($[ATP]_{mito}$) reflects mitochondrial ATP production far more sensitively than the cytosolic ATP concentration (8). Therefore, we next assessed the effect of Higd1a on ATP production in living cells using the FRET-based mitochondrial ATP biosensor Mit-ATeam (19). First, we examined the effect of KCN, an inhibitor of CcO. KCN significantly reduced the $[ATP]_{mito}$ (Fig. S7), suggesting that Mit-ATeam provides an effective means to monitor the functional consequences of changes in CcO activity. We then confirmed that hypoxia caused a gradual decline in $[ATP]_{mito}$. Overexpression of Higd1a alleviated the decline in $[ATP]_{mito}$ during hypoxia, whereas knockdown of Higd1a accelerated the decrease in $[ATP]_{mito}$ relative to the control (Fig. 4*A*).

The yeast homolog Rcf1 plays a role in respiratory supercomplex stability, and the same is true for Higd2a, but not Higd1a (11). We investigated whether Higd1a affects respiratory supercomplex stability Higd1a-knockdown or -overexpressing cells. As shown in Fig. S8, there was no significant change in the abundance or composition of the respiratory supercomplex, suggesting that the effect of Higd1a described above is not a result of changes in supercomplex stability.

Finally, to test whether the effects of Higd1a on mitochondrial ATP synthesis affected overall cell viability, we analyzed the viability of cardiomyocytes subjected to hypoxia. Under hypoxic conditions, Higd1a-knockdown cells showed a significant increase in cell death, and this effect was rescued by exogenous expression of Higd1a (Fig. 4*B* and Fig. S9*A*). In addition, overexpression of Higd1a alone

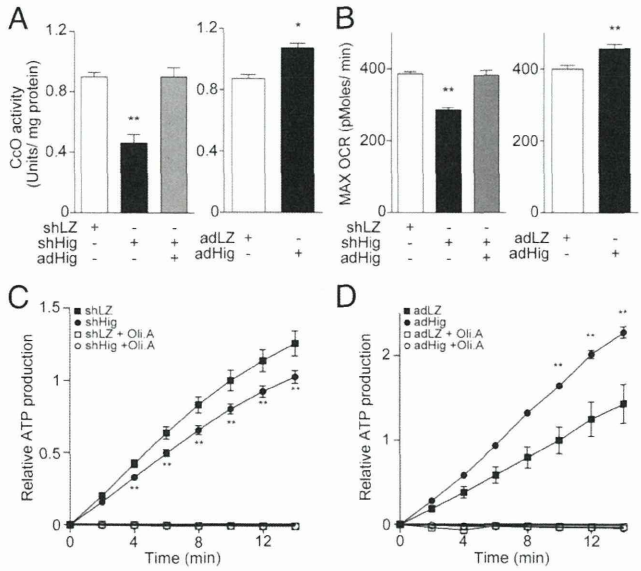

Fig. 3. Higd1a positively modulates mitochondrial respiration by altering CcO activity. (*A*, *Left*) Mitochondrial fraction from rat cardiomyocytes expressing shLacZ (shLZ), shHigd1a (shHig), or both shHig and adHigd1a (adHig) were subjected to the CcO activity assay. (*Right*) CcO activity was measured in cardiomyocytes treated with either adLacZ (adLZ) or adHig. Data represent the means of four individual experiments. (*B*, *Left*) The maximum oxygen consumption rate (max OCR) in rat cardiomyocytes transfected with the indicated adenovirus was measured after treatment with oligomycin A and fluorocarbonyl cyanide phenylhydrazone (FCCP). Knockdown of Higd1a resulted in a significant decrease in max OCR, which was rescued by exogenously expressed Higd1a. (*Right*) Overexpression of Higd1a significantly increased max OCR compared with the cells with adLZ ($n = 20$ for each group). (*C*) The relative ATP production rate of cardiomyocytes treated with shLZ or shHig was measured by the MASC assay ($n = 6$). A numerical value of ATP production at 10 min in shLZ groups is regarded as 1.0. (*D*) The relative ATP production rate of cardiomyocytes treated with adLZ or adHig was measured by MASC assay ($n = 5$). A numerical value of ATP production at 10 min in adLZ groups is regarded as 1.0. Data represent the means ± SEM; $^{*}P < 0.05$, $^{**}P < 0.01$.

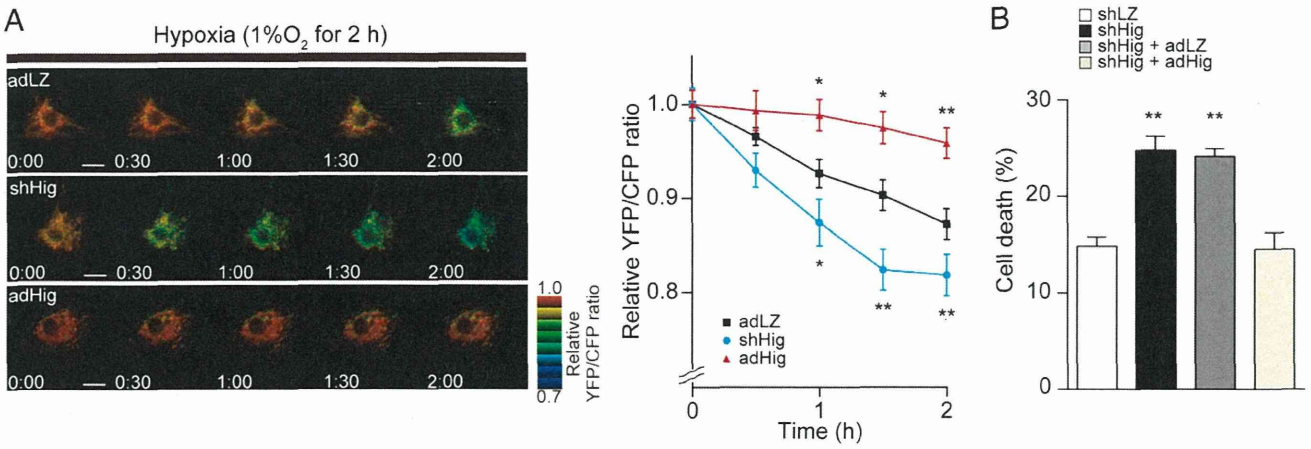

Fig. 4. (*A*) Representative sequential YFP/CFP ratiometric images of Mit-ATeam fluorescence in cardiomyocytes expressing corresponding adenovirus during hypoxia ($n = 12$ for adLZ, $n = 23$ for shHig, $n = 18$ for adHig). All of the measurements were normalized to the ratio at time 0 and compared between adLZ and adHig or shHig. (Scale bar, 20 μm.) (*B*) Cell death of cardiomyocytes treated with shHig was significantly increased compared with the control, which was rescued by addition of adHig under hypoxic conditions for 24 h ($n = 12$ for each group). Data represent the means of three independent cultures, ± SEM; $*P < 0.05$, $**P < 0.01$, compared with control (adLZ or shLZ).

increased cellular tolerance to hypoxia (Fig. S9*B*). On the basis of these findings, we conclude that Higd1a positively regulates CcO activity and subsequently increases mitochondrial ATP production, thereby protecting cardiomyocytes against hypoxia.

Discussion

In this study, we demonstrated that recombinant Higd1a produced in *Escherichia coli* was incorporated into CcO complex purified from bovine heart. The data suggest that Higd1a directly bound to the already assembled CcO complex and increased its activity. Together with the fact that Higd1a expression was rapidly increased by hypoxia, this observation indicated that Higd1a is a positive regulator of CcO that preserves the proton-motive force under hypoxic cellular stress. Physiologically, Higd1a preserved ATP production in healthy cardiomyocytes under hypoxic conditions, which protected them from an energy crisis leading to cell death.

We demonstrated that Higd1a incorporated into the CcO complex and increased its activity. It remains unclear which part of CcO is essential for this change. Higd1a binding may affect the interaction of cytochrome *c* with CcO, modulate internal electron/proton transfer, or modify K_d/K_m for O_2 binding to Cu_B/heme a_3. In fact, the resonance Raman spectroscopy experiment provided us with a clue to this question. First, we discovered that Higd1a markedly shifted the maximum Soret peak around 413 nm absorption, suggesting the occurrence of structural changes in heme that are usually observed during the reduction and oxidation process of CcO. This shift in absorbance prompted us to perform resonance Raman analysis at 413 nm excitation, a powerful tool for investigating the structure of heme and its vicinity. Higd1a induced a frequency shift of the band at 1,592 cm^{-1} to 1,562 cm^{-1} and 1,673/1,644 cm^{-1}; the former frequency is attributed to partial conversion of heme from a low-spin to a high-spin state. In oxidized CcO, only heme *a* includes low-spin iron (16); therefore, heme *a*, but not heme a_3, is responsible for this band shift.

X-ray structural and mutational analyses for bovine heart CcO have demonstrated that protons are pumped through the hydrogen-bond network across the CcO molecule, designated the H pathway, located near heme *a* (20). The driving force for active proton transport is electrostatic repulsion between the proton in the hydrogen-bond network and the net positive charge of heme *a*. One of the critical sites for repulsion is the formyl group of heme *a*, which is hydrogen bonded to Arg38 of the CcO subunit I (21). In our study, resonance Raman spectroscopy revealed specific band shifts from 1,644 cm^{-1} to 1,673 cm^{-1}, which can be attributed to the vibration of the formyl group of heme *a*. This observation suggests that Higd1a binding causes structural changes, particularly around heme *a*, weakening the hydrogen bond between the formyl group and Arg38 of the CcO subunit I, thereby leading to the acceleration of proton pumping efficiency (22). Thus, both band shifts suggest that structural change occurs in the vicinity of heme *a* rather than a_3.

Following the resonance Raman analysis, we sought to determine the Higd1a-CcO binding site via simulation with the COOT software (23), using the previously reported structures of CcO (14) and Higd1a (24). From our structural analysis, CcO contains a cleft composed of relatively few protein subunits near the active centers (Fig. S10*A*). Notably, Higd1a was predicted to integrate into the cleft of CcO near heme *a* and Arg38 (Fig. S10), consistent with the

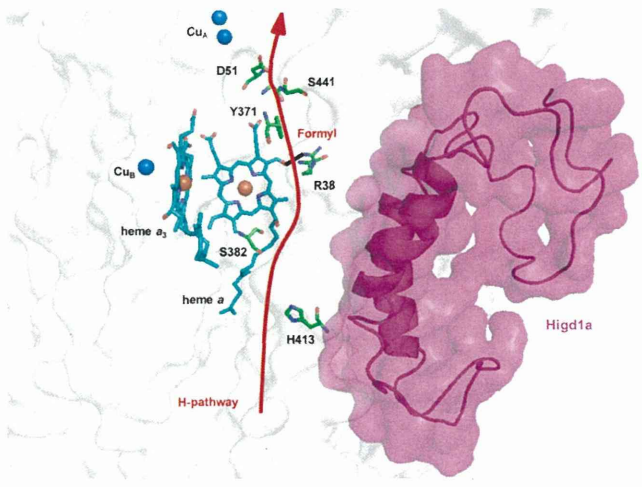

Fig. 5. Higd1a acts on the H pathway. Model depicting our docking simulation (side view) and its relationship with the H pathway. The model shows the location of Higd1a (magenta) in the CcO complex (white) and its relationship to R38 of cytochrome *c* oxidase subunit I and the formyl group of heme *a*, a component of the H pathway (red arrow).

results of the resonance Raman analysis. Thus, it is likely that Higd1a bound to the cleft of CcO, leading to swift structural change around heme *a* and Arg38 and accelerating the proton-pumping H pathway, thereby increasing CcO activity (Fig. 5). Furthermore, when we retrospectively reviewed the purification process of the CcO complex, comprising 13 subunits from the bovine heart, we found that Higd1a remained associated with CcO up to the final step, which required detergent exchange (14). This led us to speculate that Higd1a represents a 14th identified subunit of CcO that is endogenously induced by hypoxia and integrates into the open cleft of CcO to positively regulate its activity. Although the resonance Raman data and docking model simulation are consistent with the idea that Higd1a binding causes structural change around heme *a*, these data are limited because of their speculative nature. Therefore, to confirm these findings, we are currently trying to crystallize the CcO-Higd1a complex to reveal the conformational changes of CcO, particularly around the heme *a* site.

Higd1a was originally identified as a mitochondrial inner membrane protein whose expression is induced by hypoxia (25). Higd1a augments cell survival under hypoxic stress in pancreatic cells (26), and it exerts its protective effect by induction of mitochondrial fission (27). The precise relationship between these reports and our data is not clear. However, our results suggest that the elevation of CcO activity by Higd1a preserves the proton-motive force, which is prerequisite for mitochondria function, thereby leading to increased mitochondrial fission and/or the prevention of apoptosis.

The existence of a direct CcO allosteric activator suggests that there is a structural basis for the intrinsic activation in the CcO complex. To explore this idea further, a screen for small compounds that simply increase the activity of highly purified CcO in vitro has been initiated. Compounds that mimic the effect of Higd1a can preserve ATP production even under hypoxic condition, and hence are expected to exert cellular protective effects particularly when OXPHOS activity is reduced. Recent work showed that lowering the activity of OXPHOS causes the cellular senescence (28), diabetes mellitus (29), and neurodegenerative diseases (30). In addition, several currently intractable mitochondrial diseases are caused by mutations in mitochondrial genes or nuclear genes that lead to dysfunction in mitochondrial OXPHOS. Notably, decreased CcO activity is most frequently observed among patients with mitochondrial diseases (31). Therefore, small compounds that mimic the effect of Higd1a will have therapeutic potential for various acute and chronic diseases including ischemic, metabolic, and mitochondrial diseases.

Materials and Methods

Purification of Recombinant Higd1a Protein. The full-length bovine *Higd1a* cDNA was purchased from GE Healthcare. Then the coding sequence of bovine *Higd1a* was cloned in-frame with an ATG start codon, in the pET21a expression vector (Novagen for overexpression in *E. coli*). A MBP was fused in-frame at the amino terminus for purification. The resulting plasmid was transformed into BL21-Star (DE3; Invitrogen), and the addition of 0.5 mM isopropyl β-D-1-thiogalactopyranoside caused the expression of MBP-Higd1a protein. The cells were sonicated and solubilized by 1% *n*-decyl-β-D-maltoside (DM). The recombinant protein was purified with amylose resin (New England Biolabs), and eluted by 20 mM maltose (pH 6.8 or 8.0, 100 mM sodium phosphate buffer containing 0.2% DM). The eluted protein was concentrated and maltose removed using Amicon Ultra-0.5 10K (Millipore).

Resonance Raman Spectroscopy. Absorption spectra of the samples were measured by a spectrophotometer (Hitachi, U3310) with the path length of 2 mm in 100 mM sodium phosphate buffer (pH 8.0) containing 0.2% DM. The reaction mixture was measured immediately and spectra were recorded every 5 min for 30 min. The protein concentration was 8 μM.

Raman scattering of the samples were measured in a cylindrical spinning cell with excitation at 413.1 nm with a Kr^+ laser (Spectra Physics, model 2060), and the incident power was 500 μW. The detector was a liquid N_2-cooled CCD detector (Roper Scientific, Spec-10: 400B/LN). Raman shifts were calibrated with indene as the frequency standard. Raman spectrum was divided by the "white light" spectrum that was determined by measuring the scattered radiation of an incandescent lamp by a white paper to compensate for the sensitivity difference of each CCD pixel and transmission curve of the notch filter to reject Rayleigh scattering. The accuracy of the peak position of well-defined Raman bands was ±1 cm^{-1}. The protein concentration was 20 μM, and the reaction mixture was incubated for 30 min, before Raman measurements.

Measurement of CcO Activity. CcO activity was measured spectrophotometrically (Shimazu, UV-2450) using a cytochrome *c* oxidase activity kit (Biochain). A total of 25 μg of mitochondrial pellets from cardiomyocytes was lysed with 1% *n*-dodecyl-β-D-maltoside (DDM), and subjected to measurement according to the manufacturer's instructions (32). Concentrations of reduced/oxidized cytochrome *c* were determined using the extinction coefficient at 550 nm of 21.84 $mM^{-1}cm^{-1}$. For in vitro measurement, cytochrome *c* (Sigma) was reduced by ascorbic acid (Wako). Recombinant MBP-Higd1a (20 μM) and hpCcO (20 μM) were incubated at 25 °C for 30 min in the presence of 0.2% DM. After incubation, the mixture and reduced cytochrome *c* were added into the assay buffer, then subjected to measurement at 30 °C (Agilent Technologies, cary300). Slopes of OD_{550} for 1 min were calculated and corrected by a value of hpCcO.

FRET-Based Measurement of Mitochondrial ATP Concentration. FRET-based measurement of mitochondrial ATP concentration in cardiomyocytes was measured as previously described (8, 33). Briefly, FRET signal was measured in cardiomyocytes infected with adenovirus encoding mit-AT1.03 with an Olympus IX-81 inverted fluorescence microscope (Olympus) using a PL APO 60×, 1.35 N.A., oil immersion objective lens (Olympus). Fluorescence emission from Mit-ATeam was imaged by using a dual cooled CCD camera (ORCA-D2; Hamamatsu Photonics) with a dichroic mirror (510 nm) and two emission filters (483/32 nm for CFP and 542/27 nm for YFP; A11400-03; Hamamatsu Photonics). Cells were illuminated using the CoolLED pE-1 excitation system (CoolLED) with a wavelength of 425 nm. Image analysis was performed using MetaMorph (Molecular Devices). The YFP/CFP emission ratio was calculated by dividing pixel by pixel (a YFP image with a CFP image after background subtraction).

Statistical Analyses. The comparison between two groups was made by *t* test (two tailed). For MASC assay, comparison was made by repeated two-way ANOVA. A value of $P < 0.05$ was considered statistically significant. Data represent mean ± SEM.

Further methods are found in *SI Materials and Methods*.

ACKNOWLEDGMENTS. We thank T. Miyazaki (Cyclex) for making antibodies; Y. Okazaki and Y. Tokuzawa (Saitama Medical University) for measurement of CcO activity by cary300; Dr. Steven Coppen for critical reading of the manuscript; S. Ikezawa, E. Takada, and H. Shingu for technical assistance; M. Kobayashi, R. Maki, and the Center for Research Education in Osaka University for MS analysis; Y. Okada for secretarial support; and H. Shimada for discussion and advice. This research was supported by the Japan Society for the Promotion of Science through the "Funding Program for Next Generation World-Leading Researchers (NEXT Program)," initiated by the Council for Science and Technology Policy; grants-in-aid from the Ministry of Health, Labor, and Welfare-Japan; grants-in-aid from the Ministry of Education, Culture, Sports, Science, and Technology-Japan; and grants-in-aid from the Japan Society for the Promotion of Science. This research was also supported by grants from Takeda Science Foundation, Japan Heart Foundation, Japan Cardiovascular Research Foundation, Japan Intractable Diseases Research Foundation, Japan Foundation of Applied Enzymology, Japan Medical Association, Uehara Memorial Foundation, Mochida Memorial Foundation, Banyu Foundation, Naito Foundation, Inoue Foundation for Science, Osaka Medical Research foundation for intractable diseases, Ichiro Kanehara Foundation, and Showa Houkoukai.

1. Tsukihara T, et al. (1996) The whole structure of the 13-subunit oxidized cytochrome c oxidase at 2.8 A. *Science* 272(5265):1136–1144.
2. Morgan JE, Vakkasoglu AS, Lanyi JK, Gennis RB, Maeda A (2010) Coordinating the structural rearrangements associated with unidirectional proton transfer in the bacteriorhodopsin photocycle induced by deprotonation of the proton-release group: A time-resolved difference FTIR spectroscopic study. *Biochemistry* 49(15):3273–3281.
3. Aoyama H, et al. (2009) A peroxide bridge between Fe and Cu ions in the O2 reduction site of fully oxidized cytochrome c oxidase could suppress the proton pump. *Proc Natl Acad Sci USA* 106(7):2165–2169.
4. Ogura T, Kitagawa T (2004) Resonance Raman characterization of the P intermediate in the reaction of bovine cytochrome c oxidase. *Biochim Biophys Acta* 1655(1-3): 290–297.

5. Yoshikawa S, et al. (1998) Redox-coupled crystal structural changes in bovine heart cytochrome c oxidase. *Science* 280(5370):1723–1729.
6. Gospodarowicz D, Abraham JA, Schilling J (1989) Isolation and characterization of a vascular endothelial cell mitogen produced by pituitary-derived folliculo stellate cells. *Proc Natl Acad Sci USA* 86(19):7311–7315.
7. Wang GL, Semenza GL (1993) General involvement of hypoxia-inducible factor 1 in transcriptional response to hypoxia. *Proc Natl Acad Sci USA* 90(9):4304–4308.
8. Kioka H, et al. (2014) Evaluation of intramitochondrial ATP levels identifies G0/G1 switch gene 2 as a positive regulator of oxidative phosphorylation. *Proc Natl Acad Sci USA* 111(1):273–278.
9. Vukotic M, et al. (2012) Rcf1 mediates cytochrome oxidase assembly and respirasome formation, revealing heterogeneity of the enzyme complex. *Cell Metab* 15(3):336–347.
10. Strogolova V, Furness A, Robb-McGrath M, Garlich J, Stuart RA (2012) Rcf1 and Rcf2, members of the hypoxia-induced gene 1 protein family, are critical components of the mitochondrial cytochrome bc1-cytochrome c oxidase supercomplex. *Mol Cell Biol* 32(8):1363–1373.
11. Chen YC, et al. (2012) Identification of a protein mediating respiratory supercomplex stability. *Cell Metab* 15(3):348–360.
12. Fukuda R, et al. (2007) HIF-1 regulates cytochrome oxidase subunits to optimize efficiency of respiration in hypoxic cells. *Cell* 129(1):111–122.
13. Pagliarini DJ, et al. (2008) A mitochondrial protein compendium elucidates complex I disease biology. *Cell* 134(1):112–123.
14. Tsukihara T, et al. (1995) Structures of metal sites of oxidized bovine heart cytochrome c oxidase at 2.8 A. *Science* 269(5227):1069–1074.
15. Wilson DF, Gilmour MV (1967) The low-temperature spectral properties of mammalian cytochrome oxidase. I. The enzyme in intact rat-liver mitochondria. *Biochim Biophys Acta* 143(1):52–61.
16. Heibel GE, Anzenbacher P, Hildebrandt P, Schäfer G (1993) Unusual heme structure in cytochrome aa3 from Sulfolobus acidocaldarius: A resonance Raman investigation. *Biochemistry* 32(40):10878–10884.
17. Babcock GT, Callahan PM (1983) Redox-linked hydrogen bond strength changes in cytochrome a: Implications for a cytochrome oxidase proton pump. *Biochemistry* 22(10):2314–2319.
18. Fujikawa M, Yoshida M (2010) A sensitive, simple assay of mitochondrial ATP synthesis of cultured mammalian cells suitable for high-throughput analysis. *Biochem Biophys Res Commun* 401(4):538–543.
19. Imamura H, et al. (2009) Visualization of ATP levels inside single living cells with fluorescence resonance energy transfer-based genetically encoded indicators. *Proc Natl Acad Sci USA* 106(37):15651–15656.
20. Muramoto K, et al. (2010) Bovine cytochrome c oxidase structures enable O2 reduction with minimization of reactive oxygens and provide a proton-pumping gate. *Proc Natl Acad Sci USA* 107(17):7740–7745.
21. Yoshikawa S, Tsukihara T, Shinzawa-Itoh K (1996) [Crystal structure of fully oxidized cytochrome c-oxidase from the bovine heart at 2.8 A resolution]. *Biokhimiia* 61(11): 1931–1940.
22. Tsukihara T, et al. (2003) The low-spin heme of cytochrome c oxidase as the driving element of the proton-pumping process. *Proc Natl Acad Sci USA* 100(26):15304–15309.
23. Emsley P, Lohkamp B, Scott WG, Cowtan K (2010) Features and development of Coot. *Acta Crystallogr D Biol Crystallogr* 66(Pt 4):486–501.
24. Klammt C, et al. (2012) Facile backbone structure determination of human membrane proteins by NMR spectroscopy. *Nat Methods* 9(8):834–839.
25. Denko N, et al. (2000) Epigenetic regulation of gene expression in cervical cancer cells by the tumor microenvironment. *Clin Cancer Res* 6(2):480–487.
26. Wang J, et al. (2006) Pancreatic beta cells lack a low glucose and O2-inducible mitochondrial protein that augments cell survival. *Proc Natl Acad Sci USA* 103(28): 10636–10641.
27. An HJ, et al. (2013) Higd-1a interacts with Opa1 and is required for the morphological and functional integrity of mitochondria. *Proc Natl Acad Sci USA* 110(32):13014–13019.
28. Horan MP, Pichaud N, Ballard JW (2012) Review: Quantifying mitochondrial dysfunction in complex diseases of aging. *J Gerontol A Biol Sci Med Sci* 67(10): 1022–1035.
29. Saxena R, et al. (2006) Comprehensive association testing of common mitochondrial DNA variation in metabolic disease. *Am J Hum Genet* 79(1):54–61.
30. Lin MT, Beal MF (2006) Mitochondrial dysfunction and oxidative stress in neurodegenerative diseases. *Nature* 443(7113):787–795.
31. Diaz F (2010) Cytochrome c oxidase deficiency: Patients and animal models. *Biochim Biophys Acta* 1802(1):100–110.
32. Berry EA, Trumpower BL (1987) Simultaneous determination of hemes a, b, and c from pyridine hemochrome spectra. *Anal Biochem* 161(1):1–15.
33. Shintani Y, et al. (2014) Toll-like receptor 9 protects non-immune cells from stress by modulating mitochondrial ATP synthesis through the inhibition of SERCA2. *EMBO Rep* 15(4):438–445.